
# Orthotropic multisurface model with damage for macromechanical analysis of masonry structures

C. Gatta, D. Addessi

PII: S0997-7538(23)00169-9
DOI: https://doi.org/10.1016/j.euromechsol.2023.105077
Reference: EJMSOL 105077

To appear in: *European Journal of Mechanics / A Solids*

Received date : 24 August 2022
Revised date : 28 June 2023
Accepted date : 9 July 2023

Please cite this article as: C. Gatta and D. Addessi, Orthotropic multisurface model with damage for macromechanical analysis of masonry structures. *European Journal of Mechanics / A Solids* (2023), doi: https://doi.org/10.1016/j.euromechsol.2023.105077.

# Orthotropic multisurface model with damage for macromechanical analysis of masonry structures

C. Gatta*, D. Addessi

*Department of Structural and Geotechnical Engineering,*
*Sapienza University of Rome*
*Via Eudossiana 18, 00184, Rome, Italy*

**Abstract**

A novel macromechanical model with damage for the analysis of masonry structures in-plane loaded is presented. The model accounts for the directional mechanical properties typically characterizing response of masonry with regular texture. Indeed, the real heterogeneous material is modeled as a fictitious homogenized medium with orthotropic elastic constitutive behavior along the masonry natural axes, identified as the parallel and normal directions to bed joints orientation. The different strength characteristics along each material axis are taken into account by properly defining a damage matrix, which accounts for failure mechanisms due to axial tensile and compressive states, as well as shear. A suitable criterion is introduced, resulting in a damage limit surface geometrically defined in the space of the damage associated variables by the intersection of two ellipsoids and an elliptic hyperboloid. The model is implemented into a finite element procedure where the mesh-dependency numerical issue is avoided by adopting a nonlocal integral formulation. Validation examples, involving simple uni-axial and bi-axial tests, as well as more complex loading conditions, are provided to prove the model performances at both material and structural scale.

*Keywords:* masonry, damage, orthotropic response, macromechanical approach, finite element, nonlocal integral regularization

## 1. Introduction

In the last decades many experimental and numerical studies were devoted to understanding and predicting the response of masonry structures, in view of their seismic assessment. In fact, masonry is the most ancient, but still widely used, construction building material. At the conventional microscopic scale, it is a composite material obtained by assembling blocks, with various nature and shape, by means of mortar layers or dry joints. Geometry, sizes, mechanical properties and arrangement of the constituent materials strongly

*Corresponding author
*Email address:* cristina.gatta@uniroma1.it (C. Gatta)

affect the global structural response. Hence, the most natural and accurate modeling approach appears to be the so called micromechanical strategy, which separately describes each masonry component and, possibly, their interaction behavior [1, 2, 3, 4, 5, 6]. Accurate geometric and constitutive descriptions are obtained at the cost of computationally expensive numerical analyses, thus restricting the applicability of such approach to the study of small elements or structural details.

Alternately, the scientific community proposed a large variety of continuum models which consider masonry as a homogenized medium where the constituents are no longer distinguishable. The homogenized material is usually modeled by resorting to the classical Cauchy continuum [7, 8, 9, 10, 11, 12, 13], but also the micropolar Cosserat was successfully applied, especially to account for the effect of the characteristic microstructure length on the masonry macroscopic response [14, 15]. Anyway, the correct identification of the constitutive behavior of the homogenized material remains an open issue due to the uncertainty in the calibration of the evolutive laws of the inner variables governing the nonlinear mechanisms. To this end, direct approaches and homogenization and multiscale procedures were applied [16, 17]. The latters deduce the material constitutive response of the homogeneous model adopted at the structural scale from the accurate analysis of a properly selected masonry representative volume element (RVE), accounting for the detailed description of components, geometry and arrangement. Weak coupling between the material and structural scale is established if a priori homogenization is performed [18, 19], whereas a stronger connection is obtained if step-by-step [20, 21, 22, 23] or adaptive [24] multiscale procedures are adopted. Instead, the direct models calibrate the material properties and evolution laws of the inelastic variables through experimental data on masonry assemblages.

Continuum approaches based on phenomenological constitutive laws capable of describing the main features of the mechanical response without resorting to the nested step-by-step RVE-based homogenization procedures are also referred to as macromechanical models. In such context, several formulations were proposed, including damage models, plasticity models, coupled damage-plasticity models and smeared-crack models [25]. Despite most of these approximate the real masonry anisotropic response with the simplified hypothesis of isotropic behavior, these models give a fair compromise between accuracy and computational effort and were successfully applied to analyze large scale structures [26, 12]. However, when dealing with periodic well-organized masonry, the assumption of isotropic response might to be too simplistic, as regular masonry exhibits substantial discrepancy between properties observed in different material directions. The pioneer experimental campaign conducted by Page et al. on running bond panels [27, 28, 29] clearly showed that mortar joints act as plane of weakness and their orientation with respect to the applied loads strongly affects the material strength. Moreover, the anisotropic response emerges already in the elastic range and, usually, reduces to an orthotropic-type. This was proved by the correlation determined experimentally by

Cavaleri et al. [30] between the ratios Young's modulus-to-Poisson's coefficient defined along head and bed joints directions, considered as masonry natural axes.

Some attempts were made to include the effect of anisotropy in macro-models. For instance, Lourenço et al. [7] proposed an orthotropic constitutive law fully based on the plasticity theory, which employs a Rankine-type and a Hill-type criterion to simulate tensile and compressive behavior, respectively. Berto et al. [8] presented an orthotropic damage model for the analysis of brittle masonry subjected to in-plane loading, assuming the masonry natural axes as damage principal axes. They considered the equivalent effective stress measures as damage associated variables, by distinguishing the positive and negative values along the directions parallel and normal to the bed joints. Moreover, for tensile states, they introduced the dependence of the damage evolution parameters on the tensile specific fracture energy.Karapitta et al. [9] adopted a smeared-crack constitutive model capable of discerning failure modes of unreinforced masonry due to tension normal and parallel to the bed joints, masonry crushing normal and parallel to the bed joints, and masonry shear under compressive vertical stress. Pelà et al. [10] developed a damage model exploiting the concept of mapped tensors from the anisotropic field to an auxiliary isotropic workspace and, then, combined the model with the crack-tracking technique to reproduce the propagation of localized cracks [31]. Similarly, Bilko and Leszek [32] established masonry constitutive response in the framework of the elasto-plasticity theory by including a generalization of the Hoffman failure criterion in plane stress state. More recently, Tisserand et al. [33] formulated an orthotropic thermodynamics-based model including damage, unilateral effect and internal sliding and friction.

The reliability of the models described above strongly depends on the adopted failure criteria, whose definition is a hard task, given the complexity of masonry mechanical response. One of the first attempt to identify a proper failure surface for brick masonry under bi-axial stresses dates back to Dhanasekar et al. [29], which defined the surface as the intersection of three elliptic cones in the space of stresses expressed in the natural axes. Stemming from this proposal, many other formulations were suggested. Berto et al. [8] modeled the material damage space as a double pyramid with rectangular base in the equivalent effective stress space. Lourenço et al. [7] composed the limiting surface by intersecting the Rankin's and Hill's yield surfaces. Syrmakezis and Asteris [34] described mathematically the surface by means of a third order polynomial, which provided satisfactory results in case of both compressive principal stresses. Further developments conducted to more complex failure criteria in order to overcome some limitations of the previous formulations. For instance, Lishak et al. [35] proposed a very intricate surface shape composed of five parts, each corresponding to different masonry failure mode. Asteris and Plevris [36] used the neural networks to approximate the limit surface in dimensionless form by obtaining an 'onion' shape. Bilko and Leszek [32] extended the approach presented in [7] considering two orthotropic Hoffman-type failure criteria. Recently,

Malena et al. [13] modified the isotropic yield function proposed by Bigoni and Piccolroaz [37] to take into account the masonry anisotropy.

Relying on the above considerations, this work presents a novel macromechanical model with damage for the analysis of masonry structures in-plane loaded. The proposed constitutive law introduces an orthotropic description of the material elastic behavior. Then, the stiffness degradation due to cracking, crushing and shear is captured by properly defining a damage matrix, written in terms of independent scalar damage variables, whose evolution is ruled by equivalent strain measures. Moreover, a suitable damage criterion is introduced to account for the variation of the mechanical properties in the different material directions. The failure criterion results into a limit surface geometrically defined by the intersect of two ellipsoids and one elliptic hyperboloid in the space of the damage associated variables. The model is implemented in a finite element (FE) code, where the typical mesh-dependency issue of the numerical solution is overcome by adopting a nonlocal integral formulation. As observed by Bazant and Jirásek [38], who presented a comprehensive survey of the nonlocal integral procedures applied in the field of plasticity and damage constitutive formulations, nonlocal models were mainly developed to: describe the nonlocal effects in presence of material heterogeneity; regularize the boundary value problem preventing ill posedness in presence of strain-softening and, then, obtain objective numerical solutions; capture size effects observed in experiments and in discrete simulations. Also, according to Bacigalupo and Gambarotta [39], nonlocal constitutive models permit to include geometric and material length scales to account for the influence of block size and prevent pathological localizations related to the strain-softening nature of the constitutive equations adopted for brittle masonry. They analyzed running bond and English bond masonry by varying the stiffness ratio between brick and mortar and evaluated the characteristic lengths associated to the shear and extensional strains. These resulted as a fraction of the periodic cell size and characterized by different values along the direction parallel and normal to the bed mortar joints.

In this work, the integral definition of the strain measures driving the damage variables evolution is introduced to regularize the problem in presence of strain-softening constitutive behavior and guarantee the mesh-independency of the FE results. The size of the region involved in the nonlocal procedure is determined by the nonlocal radius governing the influence of the Gaussian weighting function.

The paper is organized as follows. Section 2 describes the adopted constitutive relationship, focusing on the proposed damage criterion and evolution laws of the damage variables. Section 3 provides some computational aspects related to the finite element formulation and regularization technique adopted. Section 4 presents the numerical applications. First, the model capability of capturing masonry nonlinear response is evaluated at material level by performing simple uni-axial monotonic and cyclic tests. Then, exploration is moved towards more complex bi-axial loading conditions. Finally, the structural response of masonry walls

is investigated comparing the obtained results, in terms of failure mechanisms and global load-displacement response curves, with those recovered from experimental investigations. Section 5 concludes with some remarks.

In the following the Voigt notation is adopted in the bi-dimensional (2D) framework, representing the second order tensors as 3-component vectors and the fourth order tensors as matrices.

## 2. Damage model

### *2.1. Damage-based constitutive law*

To account for masonry anisotropic macroscopic response, the real heterogeneous material is modeled as a fictitious 2D orthotropic medium under plane stress assumptions and the hypothesis of small displacements and strains. The material/intrinsic axes $(T, N)$, parallel and normal to the direction of bed joints, are considered as axes of orthotropy. First, the constitutive law is defined in the reference system $T$-$N$, then, it is expressed in the global coordinate system $X$-$Y$, by applying standard transformation rules (see Figure 1). The relation between stresses, $\boldsymbol{\Sigma}_{TN}$, and strains, $\mathbf{E}_{TN}$, referred to the material system, and the corresponding global quantities, $\boldsymbol{\Sigma}_{XY}$ and $\mathbf{E}_{XY}$, classically results as:

$$\boldsymbol{\Sigma}_{XY} = \boldsymbol{\Phi}\boldsymbol{\Sigma}_{TN} \,, \qquad \mathbf{E}_{XY} = \boldsymbol{\Psi}\mathbf{E}_{TN} \,, \tag{1}$$

where $\boldsymbol{\Phi}$ and $\boldsymbol{\Psi}$ are the rotation matrices expressed as:

$$\boldsymbol{\Phi} = \begin{bmatrix} m^2 & n^2 & -2mn \\ n^2 & m^2 & 2mn \\ mn & -mn & m^2 - n^2 \end{bmatrix} , \quad \boldsymbol{\Psi} = \begin{bmatrix} m^2 & n^2 & -mn \\ n^2 & m^2 & mn \\ 2mn & -2mn & m^2 - n^2 \end{bmatrix} , \tag{2}$$

being $m = \cos\vartheta$ and $n = \sin\vartheta$, with the angle $\vartheta$ measured counter clockwise from $X$- to $T$-axis.

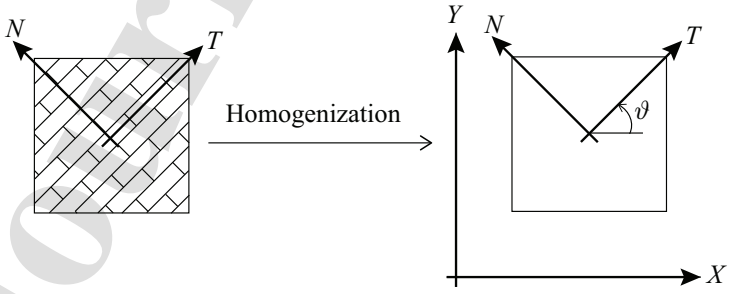


Figure 1: Material ($T$, $N$) and global ($X$, $Y$) axes of the orthotropic masonry material.

The stress-strain relationship is defined as:

$$\mathbf{\Sigma}_{TN} = (\mathbf{I} - \mathbf{D})\mathbf{C}_{TN}(\mathbf{I} - \mathbf{D})^T\mathbf{E}_{TN} = \tilde{\mathbf{C}}_{TN}\mathbf{E}_{TN} \ , \tag{3}$$

with the 2D strain vector $\mathbf{E}_{TN} = \{\mathrm{E}_T \, \mathrm{E}_N \, \Gamma_{TN}\}^T$ collecting the axial elongations along $T$ and $N$ directions, $\mathrm{E}_T$ and $\mathrm{E}_N$, and the shear strain $\Gamma_{TN}$. The stress vector $\mathbf{\Sigma}_{TN} = \{\Sigma_T \, \Sigma_N \, \Sigma_{TN}\}^T$ contains the work-conjugate quantities. $\tilde{\mathbf{C}}_{TN}$ is the effective material stiffness matrix deduced by the energy equivalence principle of damage mechanics [40], which, unlike the strain equivalence concept, leads to symmetric stiffness matrix for any damage operator [41, 42]. According to formulas in (1), the constitutive effective matrix in the global system, $\tilde{\mathbf{C}}_{XY}$, is computed as:

$$\tilde{\mathbf{C}}_{XY} = \mathbf{\Phi}\tilde{\mathbf{C}}_{TN}\mathbf{\Psi}^{-1} \ . \tag{4}$$

In Eq. (3) $\mathbf{C}_{TN}$ is the orthotropic elastic constitutive matrix of the undamaged material, depending on the Young's and shear moduli, $E_T$, $E_N$ and $G_{TN}$, and Poisson's ratios, $\nu_{TN}$, $\nu_{NT}$, $\mathbf{I}$ is the $3 \times 3$ identity matrix and $\mathbf{D}$ is the $3 \times 3$ damage operator which is defined as follows:

$$\mathbf{D} = \begin{bmatrix} D_T & 0 & 0 \\ 0 & D_N & 0 \\ 0 & 0 & D_{TN} \end{bmatrix} , \tag{5}$$

being $D_T$, $D_N$ and $D_{TN}$ three scalar damage variables. It is worth mentioning that principal values of damage are defined in most of anisotropic damage models and, consequently, damage affecting shear components results a proper combination of these quantities [41, 43, 8, 44]. Here, following the approach presented in [45, 46] for fiber-reinforced and layered composites, an independent damage variable in shear, $D_{TN}$, is introduced. This assumption can be justified by the different damaged areas for normal and shear stresses and allows for higher model versatility.

As concerns the damage variables $D_T$ and $D_N$, these are defined on the basis of damage parameters accounting for tensile, $D_{it}$, and compressive, $D_{ic}$, $(i = T, \, N)$ strain states, as follows:

$$\begin{aligned} D_T &= \alpha_T D_{Tt} + (1 - \alpha_T) D_{Tc} \ , \\ D_N &= \alpha_N D_{Nt} + (1 - \alpha_N) D_{Nc} \ . \end{aligned} \tag{6}$$

The weighting coefficients $\alpha_T$ and $\alpha_N$, defined later on, are introduced to describe the unilateral stiffness recovery due to the re-closure of the tensile cracks under compressive states during cyclic loading histories. In other words, the material degradation is irreversible but its effect on the mechanical response can be activated or inactivated depending on the applied load [10, 14, 11].

According to their physical meaning, all damage parameters, $D_{it}$, $D_{ic}$ $(i = T, N)$ and $D_{TN}$, can range between 0 and 1, representing the undamaged and completely degraded state, respectively. Moreover, the irreversible thermodynamic condition is enforced, such that $\dot{D}_{it} \geq 0$, $\dot{D}_{ic} \geq 0$ and $\dot{D}_{TN} \geq 0$, together with the physical constraint $D_{it} \geq D_{ic}$ $(i = T,\ N)$. Each damage variable is associated to a distinct failure mode, as clearly shown in Figure 2 by the typical cracking patterns due to tensile and compressive states along each natural axis, and shear state. Accordingly, associated variables $Y_i$ $(i = T,\ N,\ TN)$ are introduced. These are equivalent strain measures ruling onset and evolution of the damage parameters, as clarified later in Section 2.2. The following expressions are assumed:

$$\begin{aligned} Y_T &= \mathrm{E}_T + \tilde{\nu}_{NT}\mathrm{E}_N \ , \\ Y_N &= \mathrm{E}_N + \tilde{\nu}_{TN}\mathrm{E}_T \ , \\ Y_{TN} &= |\Gamma_{TN}| \ , \end{aligned} \tag{7}$$

where $\tilde{\nu}_{NT} = [(1 - D_N)/(1 - D_T)]\nu_{NT}$ and $\tilde{\nu}_{TN} = [(1 - D_T)/(1 - D_N)]\nu_{TN}$ are the degraded Poisson ratios, introduced to independently describe the axial damaging processes under uni-axial stress states along the material axes. From Eq. (7) it is clear that cracking and crushing failure modes, associated to $Y_T$ and $Y_N$, depend on normal strains, whereas shear failure is solely controlled by shear deformation.

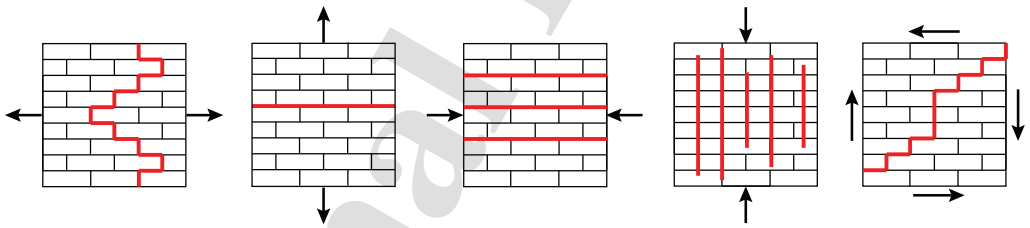


Figure 2: Schematic representation of failure modes associated to (a) $D_{Tt}$, (b) $D_{Nt}$, (c) $D_{Tc}$, (d) $D_{Nc}$ and (e) $D_{TN}$ .

On the basis of quantities in Eq. (7), the weighting coefficients $\alpha_T$ and $\alpha_N$ in Eq. (6) are expressed as:

$$\alpha_i = H(Y_i) \qquad \text{with} \quad i = (T, N) \ , \tag{8}$$

with $H(\bullet)$ denoting the Heaviside function (i.e. $H(\bullet) = 1$ if $\bullet \geq 0$, otherwise $H(\bullet) = 0$). It emerges that the model assumes no crack re-closure effect associated to $D_{TN}$, as shear damage is caused mainly by transverse cracks which do not close under reversal shear loads.

*2.2. Damage onset and evolution*

The definition of a proper failure criterion and evolution laws for the inelastic variables is a fundamental step to predict load bearing capacity of regular masonry. Inspired by the pioneer work of Dhanasekar et al. [29], the adopted damage criterion accounts for the material state referring to the natural axes. Indeed, the proposed limit surface is geometrically defined by the intersect of two ellipsoids, $F_1^D$ and $F_3^D$, and one elliptic hyperboloid, $F_2^D$, in the space of the damage associated variables. Few material parameters are needed to construct the surface, that is the initial uni-axial damage thresholds in the directions tangential, $Y_{Tt0}$ and $Y_{Tc0}$, and normal, $Y_{Nt0}$ and $Y_{Nc0}$, to the bed joints, by distinguishing them to account for the non-symmetric behavior in tension and compression (as the subscripts '$t$' and '$c$' indicate), and the pure shear threshold $Y_{s0}$. Figure 3 shows the 3D representation of the damage limit surface in the positive $Y_{TN}$-semi space (Fig. 3(a)) and two sections corresponding to $Y_{TN} = 0$ and $Y_T = Y_N$ where the mentioned thresholds are indicated (Fig. 3(b,c)). Dashed black lines in Figures 3(b,c) identify the three regions of the space in which each surface $F_i^D$ $(i = 1, 2, 3)$ defines the limit function. The resulting domain represents the damage limit surface: inner points correspond to material elastic states, points lying on the boundary indicate the onset of possible damaging mechanisms and require evolution of the surface so that the updated material states belong to the new surface boundary.

The ellipsoids $F_1^D$ and $F_3^D$, ruling states of bi-axial tension and compression coupled to shear, are expressed as:

$$F_1^D = \left(\frac{Y_T}{A_1}\right)^2 + \left(\frac{Y_N}{B_1}\right)^2 + \left(\frac{Y_{TN}}{C_1}\right)^2 - 1 \,, \tag{9}$$

$$F_3^D = \left(\frac{Y_{\alpha A}}{A_3}\right)^2 + \left(\frac{Y_{\alpha B}}{B_3}\right)^2 + \left(\frac{Y_{TN}}{C_3}\right)^2 - 1 \,, \tag{10}$$

with:

$$\begin{aligned} Y_{\alpha A} &= \quad \cos\alpha\,(Y_T - O_T) + \sin\alpha\,(Y_N - O_N) \;, \\ Y_{\alpha B} &= -\sin\alpha\,(Y_T - O_T) + \cos\alpha\,(Y_N - O_N) \;. \end{aligned} \tag{11}$$

At the onset of the damaging process, $A_1 = Y_{Tt0}$, $B_1 = Y_{Nt0}$, $B_3 = \sqrt{Y_{Tc0}^2 + Y_{Nc0}^2}/2$ and $A_3 = \beta\, B_3$, with $\beta$ the material parameter affecting the shape of the limit surface in compression (Fig. 3(b,c)). In Eq. (11), $O_T$ and $O_N$ are the coordinates of the central point $\mathbf{O} = (O_T, O_N, 0)$ of $F_3^D$ and $\alpha$ is the angle defined on the basis of the uni-axial compressive thresholds, as illustrated in Figure 3(b). Finally, quantities $C_1$ and $C_3$ in Eqs. (9) and (10) are determined so as to properly connect the two ellipsoids to $F_2^D$. This latter is defined as:

$$F_2^D = A_2\, Y_T^2 + B_2\, Y_N^2 + C_2\, Y_{TN}^2 - D_2\, Y_T\, Y_N + E_2\, Y_T + F_2\, Y_N - 1 \,, \tag{12}$$

with

$$A_2 = \frac{1}{Y_{Tt0}\, Y_{Tc0}}\,, \qquad B_2 = \frac{1}{Y_{Nt0}\, Y_{Nc0}}\,, \qquad C_2 = \frac{1}{Y_{s0}^2}\,,$$
$$D_2 = \left(\frac{1}{Y_{Tt0}\, Y_{Tc0}} + \frac{1}{Y_{Nt0}\, Y_{Nc0}}\right)\,, \qquad E_2 = \frac{Y_{Tc0} - Y_{Tt0}}{Y_{Tc0}\, Y_{Tt0}}\,, \qquad F_2 = \frac{Y_{Nc0} - Y_{Nt0}}{Y_{Nc0}\, Y_{Nt0}}\,. \tag{13}$$

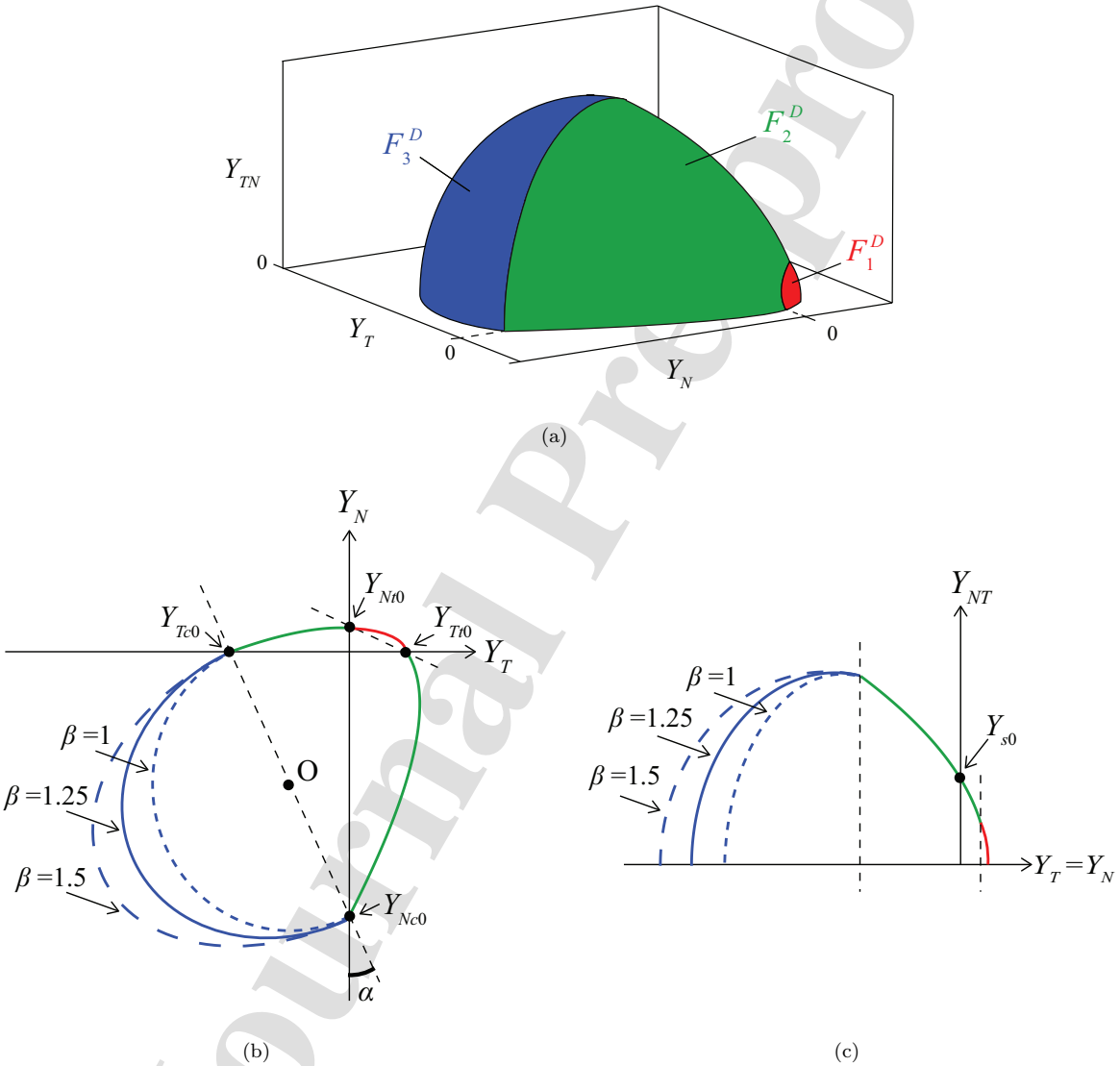


Figure 3: Damage limit surface at the onset of the damaging mechanism: (a) 3D representation, (b) and (c) sections.

Region outside the damage domain represents no admissible material states. The limit surface evolution, satisfying admissibility conditions of the material states, follows a not homothetic transformation, as illus-

trated for some examples in Figure 4. Here, for the sake of simplicity, null shear strains are considered and the surface evolution is plotted only in the $Y_T$-$Y_N$ plane. Extension to the 3D case is straightforward.

In Figure 4(a) the black square point denotes a case for which evolution of damage surface occurs. The point is characterized by $Y_T > 0$, $Y_N < 0$ and $Y_{TN} = 0$ and, consequently, only the tangential tensile, $Y_{Tt0}$, and normal compressive, $Y_{Nc0}$, thresholds evolve through the parameter $A$ (with $A \geq 1$) properly determined, keeping constant $Y_{Tc0}$, $Y_{Nt0}$ and $Y_{s0}$. The corresponding limit surface after evolution is shown in Figure 4(b) with dashed lines. Obviously, various combination of strain states can occur, leading to different types of domain evolution. For instance, in Figures 4(c) and (d) the cases of bi-axial tension and uni-axial compression along $T$-axis are illustrated.

The solution of the nonlinear evolution problem of damage variables requires to distinguish between damage in tension and compression along each material axis on the basis of the sign of $Y_i$ ($i = T, N$), and evaluate the current damage thresholds, $Y_{T0}$, $Y_{N0}$ and $Y_{TN0}$, following the procedure illustrated in Figure 4(a). The threshold quantities coincide with the coordinates of the point given by the intersection between the damage surface and the line connecting the axes origin and the material point exceeding the surface and, consequently, these can vary during the loading history due to the evolution of the damage limit domain. Once evaluated the thresholds, the following evolutive rules are adopted:

$$\dot{D}_{it} = \frac{Y_i - Y_{i0}}{Y_i + b_{it}\, Y_{i0}} \quad (Y_i \geq 0), \qquad \dot{D}_{ic} = \frac{|Y_i| - |Y_{i0}|}{|Y_i| + b_{ic}\, |Y_{i0}|} \quad (Y_i < 0), \qquad \dot{D}_{TN} = \frac{Y_{TN} - Y_{TN0}}{Y_{TN} + b_{TN}\, Y_{TN0}}, \tag{14}$$

with $i = T, N$ and $b_{Tt}$, $b_{Nt}$, $b_{Tc}$, $b_{Nc}$, $b_{TN}$ material parameters governing the growth rate of the damaging processes: the higher the parameters, the slower the damage progression and greater the resistance and fracture energy density of the material. As an example, Figure 5 shows the effect of the parameter $b_{Tt}$ on both the evolution of the corresponding damage parameter with respect to the associated variable (Figure 5(a)) and the uni-axial tensile stress-strain relationship (Figure 5(b)). Detailed description of the time discretization algorithm developed for the damage evolution problem is provided in Section 3.2.

To summarize, the proposed model requires to define, in addition to the elastic parameters, six parameters related to the damage criterion ($Y_{Tt0}, Y_{Tc0}, Y_{Nt0}, Y_{Nc0}, Y_{s0}, \beta$) and five parameters associated to the evolutive laws of the damage variables ($b_{Tt}, b_{Tc}, b_{Nt}, b_{Nc}, b_{TN}$). The resulting number of nonlinear parameters to be identify is comparable, and generally lower, to that required by other macromodels which take into account the anisotropic nonlinear response of masonry [7, 8, 9, 10].

The flexibility of the model in reproducing various shapes of the constitutive stress-strain relationships could be further improved. In fact, although the peak strengths are strongly affected by the defined damage thresholds, a limit of the current formulation is that both the peak strengths and the fracture energy densities depend on the $b_i$ ($i = Tt, Tc, Nt, Nc, TN$) parameters. Hence, the evolutive laws of the damage variables

could be modified to make the definition of strengths and fracture energies properties independent, but this would increase the number of parameters to be defined and the model complexity.

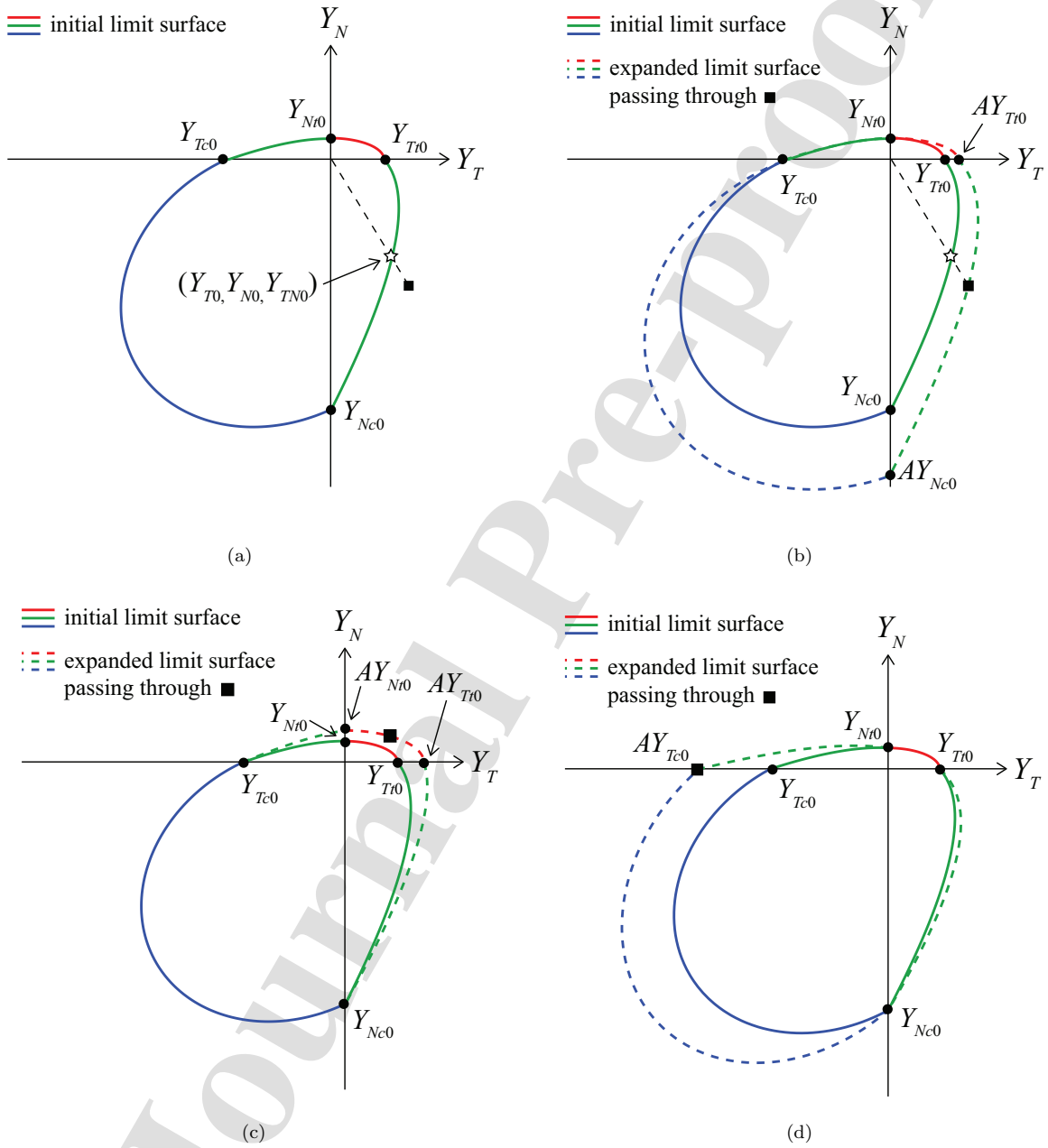


Figure 4: Evolution of the damage surface considering different material states: (a,b) combined tension along $T$-axis and compression along $N$-axis, (c) bi-axial tension and (d) uni-axial compression. Solid and dashed lines refer to the initial and expanded damage surface, respectively.

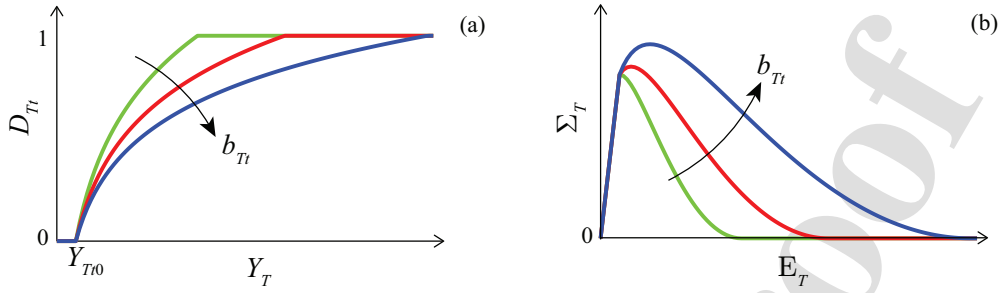


Figure 5: Effect of the material parameter $b_{Tt}$ on: (a) evolution of the damage parameter with respect to the corresponding associated variable and (b) stress-strain relationship.

## 3. Computational aspects

### *3.1. Nonlocal FE formulation*

The model presented in the previous section was introduced in a 4-node isoparametric quadrilateral elements, and implemented in a finite element procedure based on the classical displacement-based formulation. Each node is provided with two displacement degrees of freedom, and bi-linear interpolation functions are used for the two translation fields, $U_X$ and $U_Y$.

As known, when modeling response of quasi-brittle materials characterized by strain-softening constitutive behavior, like masonry, the pathological mesh-dependence problem arises. Indeed, the strain may localize into narrow bands, whose width depends on the finite element size. To overcome this numerical issue several strategies were proposed based on the fracture energy concept [47, 21, 48], higher-order formulations [49], Cosserat continuum [50, 14] and nonlocal integral approach [51, 20, 11]. Among these, the last mentioned technique is adopted in this study, as it allows to obtain objective numerical results and relies on mechanical evidences.

Giving up the principle of local action, it is assumed that the degrading process at each material point is influenced by the mechanical state of the points lying in a properly defined neighborhood. Hence, the integral definition of the damage associated variables in Eqs. (7) is introduced as:

$$\bar{Y}_i(\mathbf{X}) = \frac{1}{\int_\Omega \psi(\mathbf{X},\mathbf{S})\, d\Omega(\mathbf{S})} \int_\Omega Y_i(\mathbf{S})\, \psi(\mathbf{X},\mathbf{S})\, d\Omega(\mathbf{S}) \qquad i = T, N, TN\ , \tag{15}$$

being $\bar{Y}_i$ the nonlocal quantities at point $\mathbf{X}$, evaluated on the basis of the corresponding local variables $Y_i$ at points placed in its neighborhood on the surface $\Omega$. The influence on $\mathbf{X}$ of the point $\mathbf{S}$ is weighted by means of the classical Gaussian function $\psi$, which, in turn, depends on the nonlocal radius $L_c$, as follows:

$$\psi(\mathbf{X},\mathbf{S}) = e^{-\left(\frac{\|\mathbf{X}-\mathbf{S}\|}{L_c}\right)^2}\ . \tag{16}$$

After computating the integral quantities in Eq. (15), these are introduced in the limit functions in Eqs. (8)-(12) and, in case, are used to solve the evolution problem of the damage variables at each integration point of the FE discretized problem, according to Eqs. (14).

### *3.2. Solution algorithm*

Table 1 summarizes the main steps involved in the solution of the damage evolution problem at the typical Gauss point of each FE, making explicit the passage from the global to the material coordinate system and vice versa. Reference is made to the generic Newton-Raphson iteration '$k$' of the current time step '$t_{n+1}$' within the global solving algorithm. In short words, the FE program provides the global nodal displacement vector $\mathbf{U}^k_{XY}$, from which the element displacements $\mathbf{U}^{e^k}_{XY}$ are extracted. Then, the strains $\mathbf{E}^k_{XY}$ are computed through the compatibility matrix $\mathbf{L}^e = \mathbf{B}\mathbf{N}^e$, obtained by applying the standard compatibility operator $\mathbf{B}$ to the shape function matrix $\mathbf{N}^e$. Afterwards, the strain vector $\mathbf{E}^k_{TN}$ and the nonlocal damage associated variables $\bar{Y}^k_i$ $(i = T, N, TN)$ are evaluated. On the basis of these, the damage evolution problem is solved by computing the damage limit functions and each damage parameter according to the following general form:

$$D^k_i = D^n_i + \Delta D^k_i \qquad i = (Tt,\, Tc,\, Nt,\, Nc,\, TN)\ , \tag{17}$$

with $D^n_i$ denoting the damage value at the previous time step $t_n$ and $\Delta D^k_i$ the damage increment evaluated at the current time $t_{n+1}$ and iteration $k$ as reported in Table 2, where apex '$^{n+1}$' is omitted for simplicity. From Table 2, it emerges that each damage increment is computed using the current damage thresholds, $Y^k_{T0}$, $Y^k_{N0}$ and $Y^k_{TN0}$, and the material parameters $b_i$ $(i = Tt, Nt, Tc, Nc, TN)$.

Finally, the solving algorithm ends with the computation of the stress vector and the effective stiffness matrix referred to the material system and, after, to the global reference system, as detailed in Table 1. To be noted is that the secant stiffness matrix is adopted in the Newton-Raphson procedure, as the material tangent stiffness is cumbersome to obtain within nonlocal integral formulations [52].

## 4. Model validation

In this section, the presented model is employed to analyze masonry response both at material and structural level. First, simple uni-axial stress tests are performed, then, the exploration is moved towards more complex bi-axial loading conditions and, finally, structural applications on shear walls are presented. The numerical results are validated by comparison with experimental outcomes.

### *4.1. Uni-axial monotonic and cyclic behavior*

Uni-axial tests are performed to show the reliability of the proposed model in describing masonry orthotropic response under monotonic and cyclic loads. Numerical simulations are performed by adopting

1. Compute strains $\mathbf{E}^k_{XY}$ starting from displacements $\mathbf{U}^{e^k}_{XY}$:
   $\mathbf{E}^k_{XY} = \mathbf{L}^e \mathbf{U}^{e^k}_{XY}$
2. Project strains $\mathbf{E}^k_{XY}$ to the material coordinate system:
   $\mathbf{E}^k_{TN} = \mathbf{\Psi}^{-1} \mathbf{E}^k_{XY}$
3. Calculate the local and nonlocal damage associated variables by using Eqs. (7) and (15)
4. Evaluate the damage limit functions according to Eqs. (9)-(12)
5. Determine the damage thresholds following the example procedure illustrated in Figure 4(a)
6. Solve damage evolution problem according to Table 2 and define damage matrix $\mathbf{D}^k$ as in Eq. (5)
7. Update the limit surface after damage following the example procedure illustrated in Figure 4
8. Compute damaged stiffness matrix $\tilde{\mathbf{C}}^k_{TN}$ and stresses $\mathbf{\Sigma}^k_{TN}$:
   $\tilde{\mathbf{C}}^k_{TN} = (\mathbf{I} - \mathbf{D}^k)\mathbf{C}_{TN}(\mathbf{I} - \mathbf{D}^k)^T$
   $\mathbf{\Sigma}^k_{TN} = \tilde{\mathbf{C}}^k_{TN} \mathbf{E}^k_{TN}$
9. Evaluate $\tilde{\mathbf{C}}^k_{XY}$ and stresses $\mathbf{\Sigma}^k_{XY}$:
   $\tilde{\mathbf{C}}^k_{XY} = \mathbf{\Phi} \tilde{\mathbf{C}}^k_{TN} \mathbf{\Psi}^{-1}$
   $\mathbf{\Sigma}^k_{XY} = \mathbf{\Phi} \mathbf{\Sigma}^k_{TN}$

Table 1: Main steps of the solution of the damage evolution problem and constitutive law at the Gauss point of the FE.

material parameters contained in Table 3 and setting $\beta = 1.5$ and $b_i = 1.5$ ($i = Tt, Nt, Tc, Nc, TN$).

The first example explores the response of a masonry element subjected to uni-axial horizontal tension (i.e. tensile load acting along the global $X$-axis applied by a displacement controlled procedure), considering three values of the orthotropy angle $\vartheta$, that is $\vartheta = 0°$, $\vartheta = 45°$ and $\vartheta = 90°$. Numerical results, in terms of stress-strain relationship, are shown in Figure 6(a) and prove the model capability of accounting for orientation of the applied load with respect to bed joints direction. Indeed, different initial elastic stiffnesses and maximum strengths are obtained for the three values of the $\vartheta$ angle adopted. This is a consequence of the stress and strain fields acting in the material axis system, which cause activation of different damaging mechanisms. With reference to Figure 6(b), it appears that the damage parameter $D_{TN}$ is activated only in case of $\vartheta = 45°$, as this is related to the shear strain $\Gamma_{TN}$. Conversely, when $\vartheta = 0°$ or $\vartheta = 90°$, damage $D_{TN}$ disappears and only damage variables $D_T$ and $D_N$ arise. In particular, $D_T$ starts and evolves when $\vartheta = 0°$ since the $T$-axis coincides with the $X$-axis, whereas $D_N$ appears in case of $\vartheta = 90°$ as a consequence of the $X$- and $N$-axis overlap.

As evident from Figure 6(b), the three damage variables, $D_T$, $D_N$ and $D_{TN}$, evolve in the same way in

IF $F_h^{D^k} < 0 \qquad (h = 1, 2, 3)$

$\Delta D_{Tt}^k = \Delta D_{Tc}^k = \Delta D_{Nt}^k = \Delta D_{Nc}^k = \Delta D_{TN}^k = 0$

ELSE

$$\Delta D_{TN}^k = \frac{\bar{Y}_{TN}^k - Y_{TN0}^k}{\bar{Y}_{TN}^k + b_{TN}\, Y_{TN0}^k} \;\rightarrow\; D_{TN}^k = min\left(D_{TN}^n + \Delta D_{TN}^k,\, 1\right)$$

IF $Y_T^k > 0$ THEN

$D_{Tc}^k = D_{Tc}^n$

$$\Delta D_{Tt}^k = \frac{\bar{Y}_T^k - Y_{T0}^k}{\bar{Y}_T^k + b_{Tt}\, Y_{T0}^k} \;\rightarrow\; D_{Tt}^k = max\left(D_{Tc}^k, min\left(D_{Tt}^n + \Delta D_{Tt}^k, 1\right)\right)$$

ELSE

$$\Delta D_{Tc}^k = \frac{|\bar{Y}_T^k| - |Y_{T0}^k|}{|\bar{Y}_T^k| + b_{Tc}\, |Y_{T0}^k|} \;\rightarrow\; D_{Tc}^k = min\left(D_{Tc}^n + \Delta D_{Tc}^k,\, 1\right)$$

$D_{Tt}^k = max\left(D_{Tc}^k,\, D_{Tt}^n\right)$

END

IF $Y_N^k > 0$ THEN

$D_{Nc}^k = D_{Nc}^n$

$$\Delta D_{Nt}^k = \frac{\bar{Y}_N^k - Y_{N0}^k}{\bar{Y}_N^k + b_{Nt}\, Y_{N0}^k} \;\rightarrow\; D_{Nt}^k = max\left(D_{Nc}^k, min\left(D_{Nt}^n + \Delta D_{Nt}^k, 1\right)\right)$$

ELSE

$$\Delta D_{Nc}^k = \frac{|\bar{Y}_N^k| - |Y_{N0}^k|}{|\bar{Y}_N^k| + b_{Nc}\, |Y_{N0}^k|} \;\rightarrow\; D_{Nc}^k = min\left(D_{Nc}^n + \Delta D_{Nc}^k, 1\right)$$

$D_{Nt}^k = max\left(D_{Nc}^k,\, D_{Nt}^n\right)$

END

END

Table 2: Solution algorithm for the evolution laws of the damage variables.

case of $\vartheta = 45°$. This is a special condition due to the parameters chosen to rule the damage evolution, that is $b_{Tt} = b_{Nt} = b_{TN}$. Indeed, different evolutive laws and constitutive responses could be obtained by removing these assumptions. To clarify, Figure 7(a) shows the stress-strain relationship and the damage variations corresponding to $b_{Tt} = b_{Nt} = 1.5$ and $b_{TN} = 2.5$. It emerges that the evolution of $D_{TN}$ differs from that of $D_T$ and $D_N$. Finally, completely different damage increments appear in the most general case, as testified in Figure 7(b), where results obtained assuming $b_{Tt} = 2.5$, $b_{Nt} = 1.5$, $b_{TN} = 3$ are reported.

In these monotonic tests damages $D_T$ and $D_N$ represent the material degradation caused by tensile load

Table 3: Material parameters for uni-axial tests in Figures 6, 7 and 8.

| Elastic parameters | | | | Damage parameters | | | | |
|---|---|---|---|---|---|---|---|---|
| $E_T$ [MPa] | $E_N$ [MPa] | $\nu_{TN}$ | $G_{TN}$ [MPa] | $Y_{Tt0}$ | $Y_{Nt0}$ | $Y_{Tc0}$ | $Y_{Nc0}$ | $Y_{s0}$ |
| 4000 | 2000 | 0.1 | 1500 | 9.95E-05 | 9.95E-05 | 7.46E-04 | 1.99E-03 | 3.33E-04 |

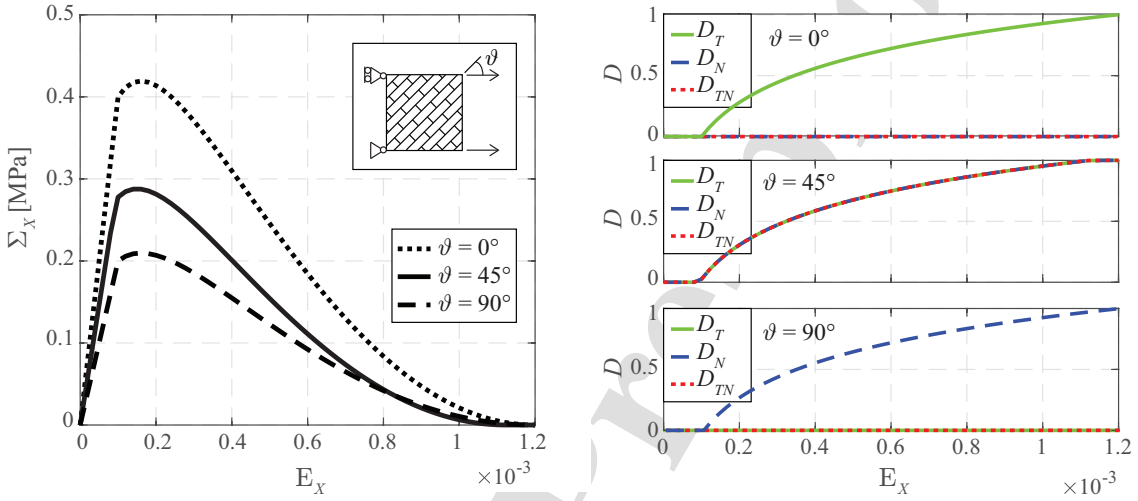


(a) (b)

Figure 6: Uni-axial tensile response for different values of the orthotropy angle $\vartheta$: (a) stress-strain relationships, (b) variations of the damage variables $D_T$, $D_N$ and $D_{TN}$ with respect to the strain $E_X$.

and, accordingly, always correspond to $D_{Tt}$ and $D_{Nt}$, respectively. Instead, when dealing with the cyclic response, it is useful decompose the damage parameters in their tensile and compressive part, especially if the re-closure crack phenomenon is to be analyzed. As an example, Figure 8(a) shows the stress-strain relationship obtained by applying the deformation history at the top of Figure 8(b) to the masonry specimen with horizontal bed joints, i.e. $\vartheta = 0°$ (it is assumed $b_{Tt} = b_{Tc} = 1.5$). It can be noticed that the stiffness recovery occurs when passing from tension to compression (A-B phase), as this is related to the re-closure of the tensile cracks under compressive states. The subsequent reloading in tension, which leads to point C, is slightly affected by the accumulated compressive damage, because of the constraint $D_{Tt} \geq D_{Tc}$. The phenomenon is clearly illustrated in the lower part of Figure 8(b), where the variations of the damage variables $D_{Tt}$, $D_{Tc}$ and $D_T$ are plotted with respect to the fictitious time variable with red, green and dashed black curve, respectively. Apparently, $D_T$ assumes the same value of $D_{Tt}$ for tensile states and, then, when a reversal strain occurs, returns equal to $D_{Tc}$, allowing a proper representation of the unilateral damage

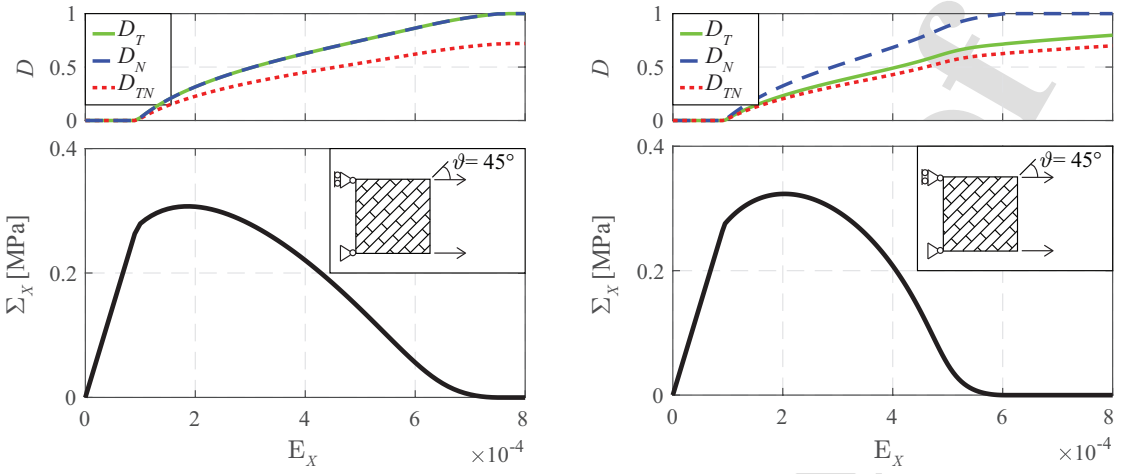


Figure 7: Uni-axial tensile stress-strain relationships and variations of the damage variables for $\vartheta = 45°$: (a) $b_{Tt} = b_{Nt} = 1.5$ and $b_{TN} = 2.5$, (b) $b_{Tt} = 2.5$, $b_{Nt} = 1.5$, $b_{TN} = 3$.

recovering upon load reversal.

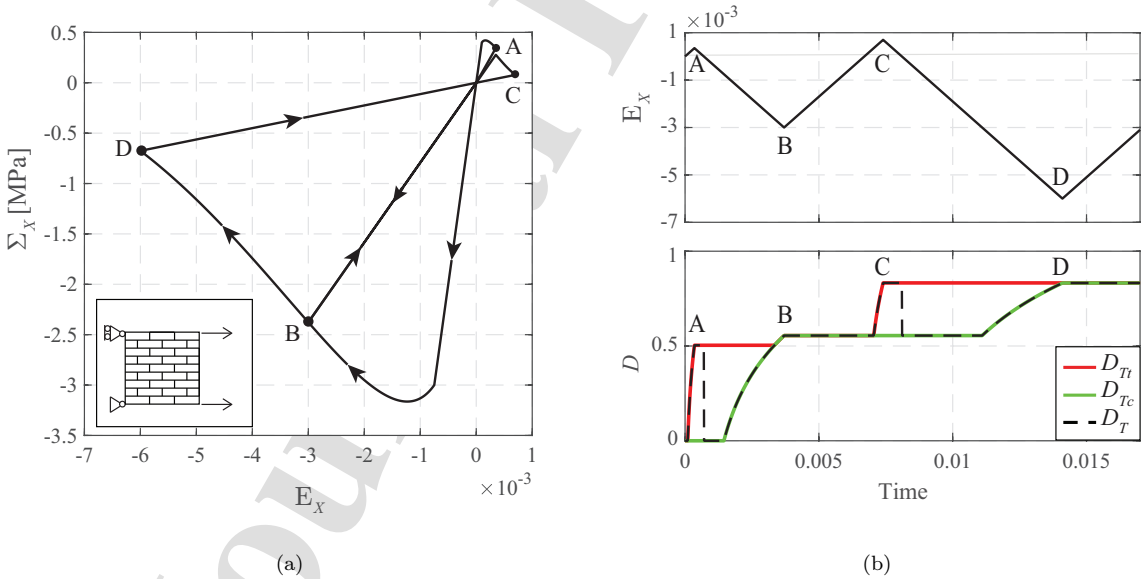


Figure 8: Uni-axial cyclic response for $\vartheta = 0°$: (a) stress-strain law, (b) evolution of the strain $E_X$ and damage variables $D_T$, $D_{Tt}$ and $D_{Tc}$ during the loading history.

### 4.2. Bi-axial response: comparison with experimental data

The experimental data provided by Page [27, 28] are used as reference solutions to study the in-plane anisotropic response of masonry. Masonry panels, made of half-scale solid clay units arranged in running bond, were tested under bi-axial loading conditions by using a proper device to impose uniform stress states. The applied loads were oriented at various angle $\vartheta$ with respect to bed joints and the resulting failure surfaces were obtained in terms of principal stresses and their orientation to the bed joints. Test results proved that mortar joints act as planes of weakness, causing distinct directional properties. This clearly emerges from Figures 9(a-c), where the experimental failure domains are depicted with dots for cases of $\vartheta = 0°$, $22.5°$ and $45°$. Results referred to $\vartheta = 67.5°$ and $\vartheta = 90°$ are implicitly contained in those of $\vartheta = 22.5°$ and $\vartheta = 0°$, respectively. Figures 9(a-c) also show the numerical failure surfaces (solid lines) derived with the proposed model adopting the material parameters contained in Table 4, set according to [27, 28, 53]. For the analyses is assumed $\beta = 1.5$ and $b_i = 2$ $(i = Tt, Nt, Tc, Nc, TN)$.

Table 4: Material parameters for bi-axial tests in Figure 9.

| Elastic parameters | | | | Damage parameters | | | | |
|---|---|---|---|---|---|---|---|---|
| $E_T$ [MPa] | $E_N$ [MPa] | $\nu_{TN}$ | $G_{TN}$ [MPa] | $Y_{Tt0}$ | $Y_{Nt0}$ | $Y_{Tc0}$ | $Y_{Nc0}$ | $Y_{s0}$ |
| 5700 | 5600 | 0.19 | 2350 | 6.8E-05 | 4.1E-05 | 6.8E-04 | 1.2E-03 | 1.9E-04 |

On the overall, a pretty good agreement emerges between experimental and numerical outcomes. In fact, according to the experimental data, the numerical surface exhibits a non-symmetric shape in case of $\vartheta = 0°$, being the compressive strengths normal and parallel to bed joints significantly different. Then, by increasing $\vartheta$, the shape of the failure domain varies. Despite some slight discrepancies between experimental and numerical data, the proposed model well describes the symmetric shape characterizing the case of $\vartheta = 45°$. These results clearly testify the model capability of accounting for the bed joints orientation relative to the principal stresses, thus describing in a phenomenological way the preferential direction of microcracks evolution due to the spatial arrangement of mortar and bricks.

### 4.3. Numerical and experimental response of shearing walls

To explore the capability of the model of reproducing response of masonry structural elements, the panels experimentally tested by Raijmakers and Vermeltfoort [54] are numerically studied. The walls were built by assembling 18 courses of solid bricks with dimensions $210 \times 52 \times 100\,\text{mm}^3$ and 10 mm thick mortar. Only 16 courses were activated, thus resulting in overall width $W = 990\,\text{mm}$ and height $H = 1000\,\text{mm}$ (Figure 10). The experiments involved two phases: first, a vertical pressure $p$ was applied on the top side, then, a monotonically increasing horizontal displacement $s$ was imposed through a steel beam, preventing any

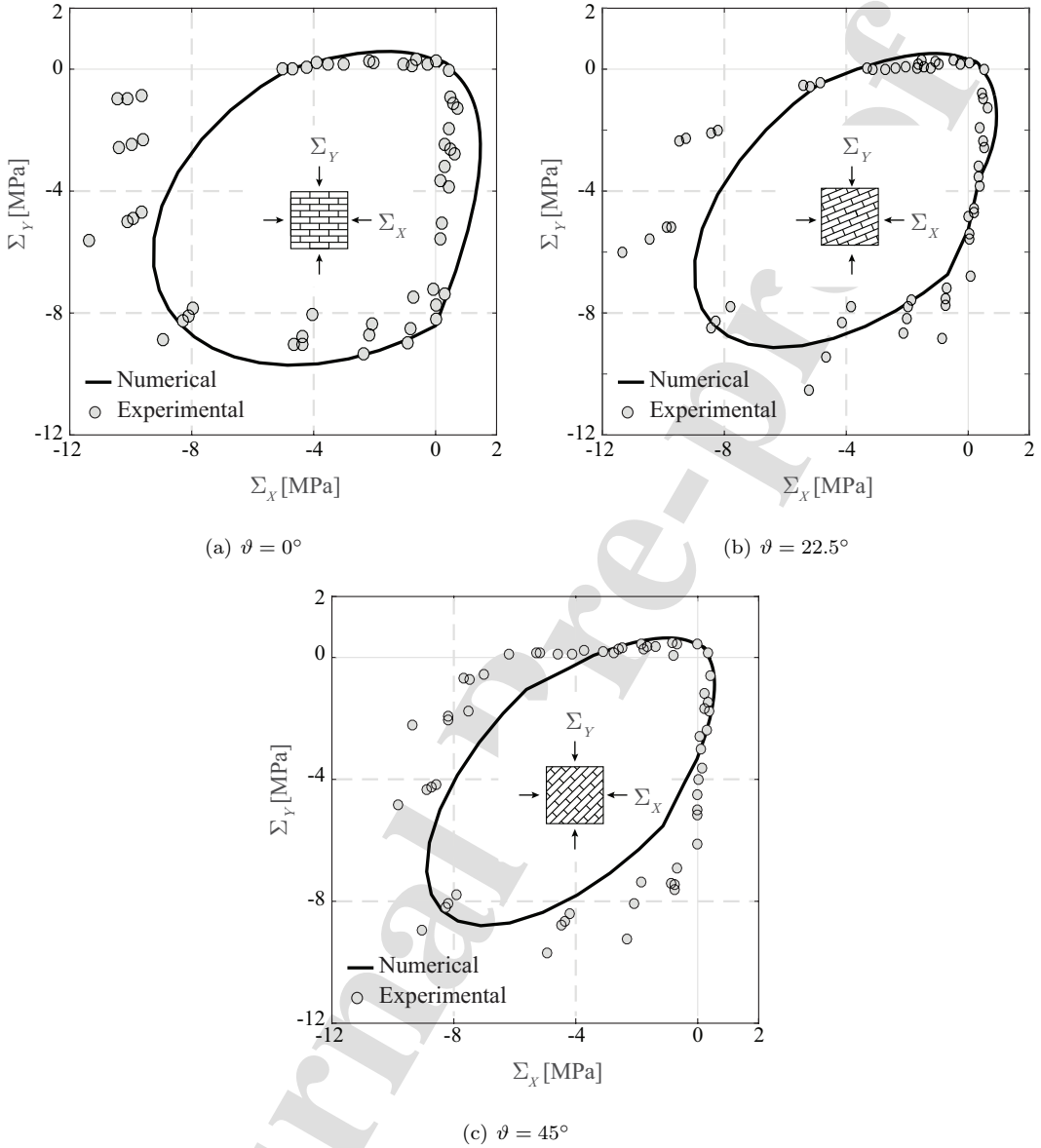


(a) $\vartheta = 0°$

(b) $\vartheta = 22.5°$

(c) $\vartheta = 45°$

Figure 9: Comparison between numerical (solid lines) and experimental (dots) [27, 28] bi-axial failure domains for different values of $\vartheta$.

335 vertical movement of the upper boundary (Figure 10). Four specimens, labeled as JD walls, were tested assuming different levels of the compression load, i.e. $p = 0.3\,\text{MPa}$ for J4D and J5D, $p = 1.21\,\text{MPa}$ for J6D and $p = 2.12\,\text{MPa}$ for J7D.

To perform the numerical simulations, the effective elastic properties of the material were derived via a homog-

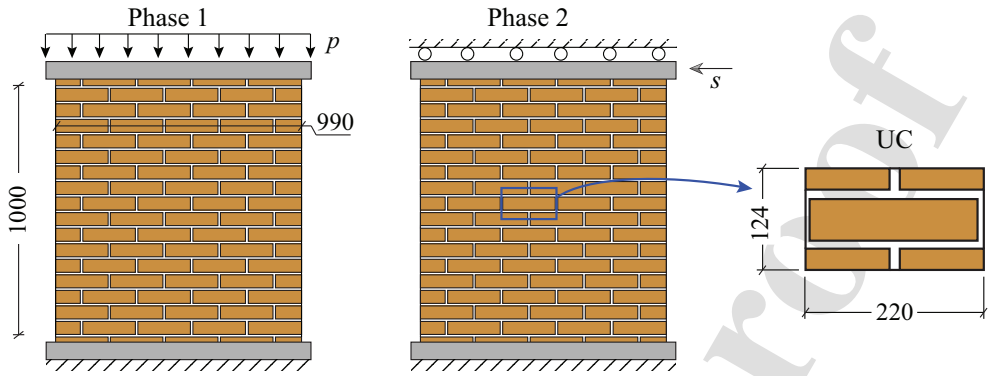


Figure 10: Test phases for Raijmakers-Vermeltfoort panels and selected masonry UC.

enization procedure. This is based on the selection of a masonry unit cell (UC) representative of the regular arrangement (UC in Figure 10), both in terms of geometric characteristics and constitutive properties of the components. The cell is modeled with 4-node quadrilateral FEs explicitly distinguishing between bricks, $'b'$, and mortar, $'m'$, for which the linear elastic isotropic behavior is assumed (Young's moduli $E_b = 16700\,\text{MPa}$ and $E_m = 800\,\text{MPa}$, Poisson ratios $\nu_b = 0.15$ and $\nu_m = 0.11$ [55, 56]). Enforcing proper periodicity conditions on the UC boundaries, the unit macroscopic strains $\mathbf{E}_{TN} = \{1\,0\,0\}^T$, $\mathbf{E}_{TN} = \{0\,1\,0\}^T$ and $\mathbf{E}_{TN} = \{0\,0\,1\}^T$ are sequentially imposed as input kinematic actions and, then, the stress field in the UC is evaluated. On the basis of this, the macroscopic stresses, $\mathbf{\Sigma}_{TN}$, associated to the imposed macroscopic strains, and representing the columns of the homogenized elastic stiffness matrix $\mathbf{C}_{TN}$, are computed by applying the Hill-Mandel principle [57]. Table 5 shows the evaluated elastic moduli and Poisson ratio of the homogenized orthotropic medium.

The nonlinear mechanical properties are identified on the basis of the experimental data and values reported in [19, 10, 13]. The corresponding model parameters, contained in Table 5, lead to the following homogenized strength properties: tensile and compressive strengths parallel to bed joints equal to 0.37 MPa and 12.7 MPa, tensile and compressive strengths normal to bed joints equal to 0.28 MPa and 10.0 MPa, and shear strength equal to 0.45 MPa (having set $\beta = 1.5$, $b_{Tt} = b_{Tc} = 2.2$, $b_{Nt} = b_{Nc} = 2.5$ and $b_{TN} = 2.3$). A mesh made of 10×10 4-node quadrilateral FEs is used to perform the numerical simulations, assuming the nonlocal radius $L_c = 220\,\text{mm}$ in accordance to brick and mesh sizes. The values of $b_i$ $(i = Tt, Tc, Nt, Nc, TN)$ and $L_c$ are set so as to obtain the required strengths properties along the different material directions and represent the characteristic length of the microstructure, respectively.

Figure 11 compares the global load-displacement curves evaluated numerically (red lines) and experimentally (black lines). It appears that the model well reproduces both the increase in peak load and brittle behavior,

with increasingly severe softening branches, as the vertical load increases. Some differences emerge between numerical and experimental outcomes in the pre-peak responses, due to some nonlinear mechanisms that are not properly reproduced by the model because they are possibly a consequence of pre-existing damage or different initial conditions. In fact, the numerical-experimental discrepancies could be significantly reduced if different mechanical parameters were assumed for the three specimens, as done in other works [19, 58]. However, the aim here is not to consider the possible variation of the macromechanical properties related to defects caused by the experimental construction process, but is to reproduce the overall behavior of the panels initially made of the same masonry material using a single set of mechanical parameters.

Table 5: Material parameters adopted for Raijmakers-Vermeltfoort panels.

| Elastic parameters | | | | Damage parameters | | | | |
|---|---|---|---|---|---|---|---|---|
| $E_T$ [MPa] | $E_N$ [MPa] | $\nu_{TN}$ | $G_{TN}$ [MPa] | $Y_{Tt0}$ | $Y_{Nt0}$ | $Y_{Tc0}$ | $Y_{Nc0}$ | $Y_{s0}$ |
| 8638.5 | 3910.3 | 0.11 | 1607.0 | 3.5E-05 | 5.1E-05 | 1.2E-03 | 1.8E-03 | 2.1E-04 |

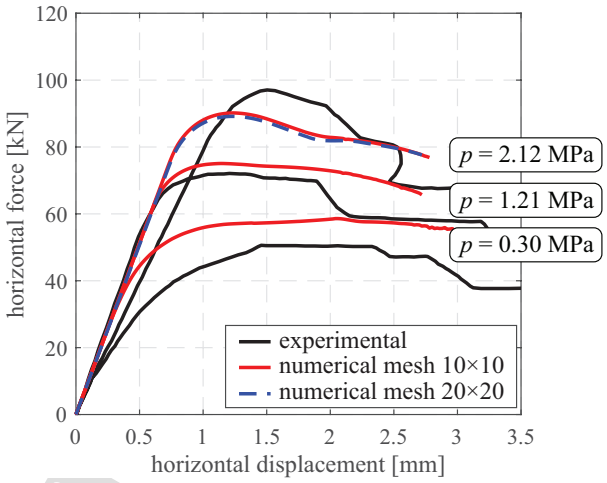


Figure 11: Comparison between experimental and numerical force-displacement curves for Raijmakers-Vermeltfoort panels.

As concerns the activated failure modes, Figure 12 shows the experimental cracking paths for all the considered values of the compression load $p$. The distributions of the damage variables derived from the numerical simulations are contained in Figures 13,14,15. Although in a smeared fashion, the model reproduces damage distributions in accordance with the experimental evidences. In fact, diagonal damaged bands in the middle of the panels and damaged zones located at the bottom and top corners of the walls, where shear and tensile strains are concentrated, respectively, emerge. To be noted is that, due to the nature of the formulated

model based on continuum damage mechanics, as well as the adoption of the nonlocal integral procedure, spread damage mechanisms are reproduced. To describe concentrated and localized fracture modes, different modeling approaches should be resorted to. As concerns the effect of the compression state, it emerges that the shear mechanism becomes more and more relevant as the value of the vertical load $p$ increases.

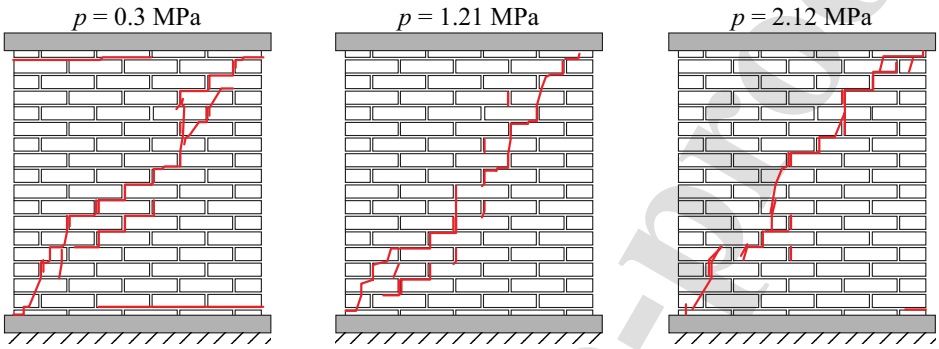


Figure 12: Raijmakers-Vermeltfoort panels: experimental cracking paths for different values of the vertical compression $p$.

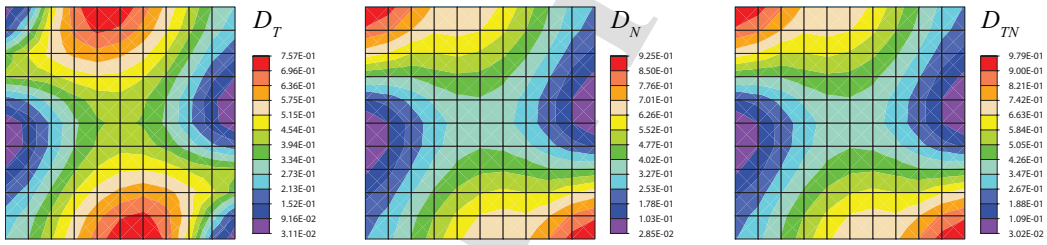


Figure 13: Raijmakers-Vermeltfoort panels: distributions of the damage variables for $p = 0.3\,\text{MPa}$ and $s = 2.2\,\text{mm}$.

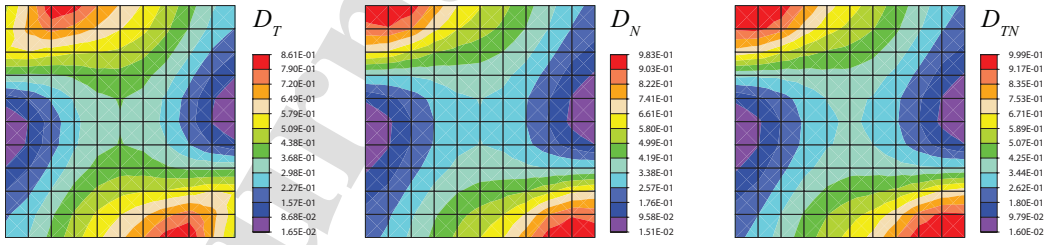


Figure 14: Raijmakers-Vermeltfoort panels: distributions of the damage variables for $p = 1.21\,\text{MPa}$ and $s = 2.2\,\text{mm}$.

380 Finally, the structural behavior of the panel characterized by the highest compression load, whose response curve exhibits the steepest softening branch, is also reproduced adopting a denser mesh made of $20\times20$ FEs. The corresponding load-displacement curve, depicted with blue dashed line in Figure 11, is indistinguishable from that evaluated with the coarser discretization consisting of $10\times10$ FEs, thus proving the efficiency of

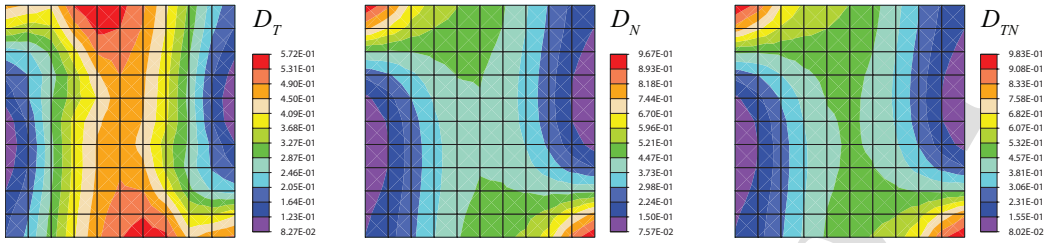


Figure 15: Raijmakers-Vermeltfoort panels: distributions of the damage variables for $p = 2.12\,\text{MPa}$ and $s = 2.2\,\text{mm}$.

the regularization technique adopted.

## 5. Conclusion

A novel macromechanical model with damage for the analysis of in-plane loaded masonry structures with regular arrangement of bricks and mortar joints was proposed. The model introduces an orthotropic description of the elastic behavior of the homogenized masonry and is based on a matrix representation of damage accounting for the variation of the strength properties observed for different material directions. Indeed, distinct damage parameters are introduced to model and distinguish degrading mechanisms due to both tensile and compressive states, as well as shear, referred to masonry natural axes (i.e. the bed and head joints directions). A suitable failure criterion is formulated by defining a multisurface damage domain geometrically given by the intersection of two ellipsoids and one elliptic hyperboloid in the space of the damage associated variables. The surface follows a not homothetic transformation during the typical loading history, thus limiting the interaction effect of the degradation of the mechanical properties in the two masonry natural directions. Despite the model relies on the hypothesis of orthotropic local behavior of the material, the overall anisotropic damaging response is, however, described by the onset and subsequent damage localization at the structural level.

The model was introduced in an isoparametric displacement-based quadrilateral element and implemented in the finite element code FEAP. A nonlocal integral formulation was adopted to obtain mesh-independent numerical solutions.

Several applications, at both material and structural scales, were performed to evaluate the performaces of the proposed model. The uni-axial tests proved the model capability of describing the different strength and stiffness characteristics along the material axes and the typical softening branches of the constitutive responses. Moreover, the effectiveness of the introduced damage limit surface was showed by comparison of numerically and experimentally evaluated bi-axial failure domains. Finally, the experimental response of shearing masonry panels subjected to different level of pre-compression load was satisfactory reproduced,

both in terms of global load-displacement curves and cracking paths. Numerical outcomes obtained with coarse and denser meshes confirmed the effectiveness of the adopted regularization technique. To be noted is that the global load-displacement response curves have to be complemented with the observation of the local distributions of strains and damage to get information on the length scale measurement.

At the present stage, the model is not able to completely reproduce the masonry cyclic response. Although the formulation considers the unilateral stiffness recovery due to the re-closure of the tensile cracks under cyclic loads, the hysteretic dissipation caused by frictional mechanisms at the interface between mortar and bricks is not taken into account. Hence, the presented modeling strategy is suitable for future developments involving the coupling of the proposed damage model with a proper plasticity formulation.

## 6. Acknowledgements

D.A. and C.G. acknowledge the grant PNRR PE5-CHANGES-Spoke 7 (CUP: B53C22003780006) and Research Project "STAND" n. POR A0375E0080.

## References

[1] D. V. Oliveira, P. B. Lourenço, Implementation and validation of a constitutive model for the cyclic behaviour of interface elements, Computers & Structures 82 (17-19) (2004) 1451–1461.

[2] D. Addessi, E. Sacco, A kinematic enriched plane state formulation for the analysis of masonry panels, European Journal of Mechanics-A/Solids 44 (2014) 188–200.

[3] D. Baraldi, E. Reccia, A. Cecchi, In plane loaded masonry walls: DEM and FEM/DEM models. A critical review, Meccanica 53 (7) (2018) 1613–1628.

[4] E. Minga, L. Macorini, B. A. Izzuddin, A 3D mesoscale damage-plasticity approach for masonry structures under cyclic loading, Meccanica 53 (7) (2018) 1591–1611.

[5] D. Addessi, P. Di Re, E. Sacco, Micromechanical and multiscale computational modeling for stability analysis of masonry elements, Engineering Structures 211 (2020) 110428.

[6] M. Nocera, C. Gatta, D. Addessi, D. Liberatore, Micromechanical modeling of unreinforced masonry arches accounting for flexural hinges and shear slidings, International Journal of Architectural Heritage (2021) 1–12.

[7] P. B. Lourenço, R. De Borst, J. G. Rots, A plane stress softening plasticity model for orthotropic materials, International Journal for Numerical Methods in Engineering 40 (21) (1997) 4033–4057.

[8] L. Berto, A. Saetta, R. Scotta, R. Vitaliani, An orthotropic damage model for masonry structures, International Journal for Numerical Methods in Engineering 55 (2) (2002) 127–157.

[9] L. Karapitta, H. Mouzakis, P. Carydis, Explicit finite-element analysis for the in-plane cyclic behavior of unreinforced masonry structures, Earthquake Engineering and Structural Dynamics 40 (2) (2011) 175–193.

[10] L. Pelà, M. Cervera, P. Roca, An orthotropic damage model for the analysis of masonry structures, Construction and Building Materials 41 (2013) 957–967.

[11] C. Gatta, D. Addessi, F. Vestroni, Static and dynamic nonlinear response of masonry walls, International Journal of Solids and Structures 155 (2018) 291–303.

[12] D. Addessi, C. Gatta, M. Nocera, D. Liberatore, Nonlinear dynamic analysis of a masonry arch bridge accounting for damage evolution, Geosciences 11 (8) (2021) 343.

[13] M. Malena, G. de Felice, S. Marfia, AnMas: Anisotropic strength domain for masonry, Engineering Structures 257 (2022) 114050.

[14] D. Addessi, A 2D Cosserat finite element based on a damage-plastic model for brittle materials, Computers & Structures 135 (2014) 20–31.

[15] M. Tuna, P. Trovalusci, Scale dependent continuum approaches for discontinuous assemblies: 'Explicit' and 'implicit' non-local models, Mechanics Research Communications 103 (2020) 103461.

[16] E. Sacco, D. Addessi, K. Sab, New trends in mechanics of masonry, Meccanica 53 (7) (2018) 1565–1569.

[17] A. M. D'Altri, V. Sarhosis, G. Milani, J. Rots, S. Cattari, S. Lagomarsino, E. Sacco, A. Tralli, G. Castellazzi, S. de Miranda, Modeling strategies for the computational analysis of unreinforced masonry structures: review and classification, Archives of Computational Methods in Engineering (2019) 1–33.

[18] A. Anthoine, Derivation of the in-plane elastic characteristics of masonry through homogenization theory, International Journal of Solids and Structures 32 (2) (1995) 137–163.

[19] G. Milani, P. B. Lourenço, A. Tralli, Homogenised limit analysis of masonry walls, Part I: Failure surfaces, Computers & Structures 84 (3-4) (2006) 166–180.

[20] S. Marfia, E. Sacco, Multiscale damage contact-friction model for periodic masonry walls, Computer Methods in Applied Mechanics and Engineering 205 (2012) 189–203.

[21] M. Petracca, L. Pelà, R. Rossi, S. Oller, G. Camata, E. Spacone, Regularization of first order computational homogenization for multiscale analysis of masonry structures, Computational Mechanics 57 (2) (2016) 257–276.

[22] D. Addessi, C. Gatta, S. Marfia, E. Sacco, Multiscale analysis of in-plane masonry walls accounting for degradation and frictional effects, International Journal for Multiscale Computational Engineering 18 (2) (2020).

[23] D. Addessi, P. Di Re, C. Gatta, E. Sacco, Multiscale analysis of out-of-plane masonry elements using different structural models at macro and microscale, Computers & Structures 247 (2021) 106477.

[24] L. Leonetti, F. Greco, P. Trovalusci, R. Luciano, R. Masiani, A multiscale damage analysis of periodic composites using a couple-stress/cauchy multidomain model: Application to masonry structures, Composites Part B: Engineering 141 (2018) 50–59.

[25] D. Fusco, F. Messali, J. G. Rots, D. Addessi, S. Pampanin, Numerical issues on brittle shear failure of pier-wall continuous vertical joints in urm dutch buildings, Engineering Structures 258 (2022) 114078.

[26] S. Tiberti, M. Acito, G. Milani, Comprehensive FE numerical insight into Finale Emilia Castle behavior under 2012 Emilia Romagna seismic sequence: Damage causes and seismic vulnerability mitigation hypothesis, Engineering Structures 117 (2016) 397–421.

[27] A. W. Page, The biaxial compressive strength of brick masonry, Proceedings of the Institution of Civil Engineers 71 (3) (1981) 893–906.

[28] A. W. Page, The strength of brick masonry under biaxial tension-compression, International Journal of Masonry Construction 3 (1) (1983) 26–31.

[29] M. Dhanasekar, A. W. Page, P. W. Kleeman, The failure of brick masonry under biaxial stresses, Proceedings of the Institution of Civil Engineers 79 (2) (1985) 295–313.

[30] L. Cavaleri, M. Papia, G. Macaluso, F. Di Trapani, P. Colajanni, Definition of diagonal Poisson's ratio and elastic modulus for infill masonry walls, Materials and Structures 47 (1-2) (2014) 239–262.

[31] L. Pelà, M. Cervera, S. Oller, M. Chiumenti, A localized mapped damage model for orthotropic materials, Engineering Fracture Mechanics 124 (2014) 196–216.

[32] P. Bilko, L. Małyszko, An orthotropic elastic-plastic constitutive model for masonry walls, Materials 13 (18) (2020) 4064.

[33] P. J. Tisserand, H. Rostagni, C. Giry, T. T. H. Nguyen, R. Desmorat, F. Ragueneau, An orthotropic damage model with internal sliding and friction for masonry-like material, Engineering Fracture Mechanics 267 (2022) 108397.

[34] C. Syrmakezis, P. Asteris, Masonry failure criterion under biaxial stress state, Journal of Materials in Civil Engineering 13 (1) (2001) 58–64.

[35] V. I. Lishak, V. I. Yagust, D. Z. Yankelevsky, 2-D orthotropic failure criteria for masonry, Engineering Structures 36 (2012) 360–371.

[36] P. G. Asteris, V. Plevris, Anisotropic masonry failure criterion using artificial neural networks, Neural Computing and Applications 28 (8) (2017) 2207–2229.

[37] D. Bigoni, A. Piccolroaz, Yield criteria for quasibrittle and frictional materials, International Journal of Solids and Structures 41 (11-12) (2004) 2855–2878.

[38] P. B. Zdeněk, M. Jirásek, Nonlocal integral formulations of plasticity and damage: Survey of progress, Journal of Engineering Mechanics 128 (11) (2002) 1119–1149.

[39] A. Bacigalupo, L. Gambarotta, Computational two-scale homogenization of periodic masonry: characteristic lengths and dispersive waves, Computer Methods in Applied Mechanics and Engineering 213 (2012) 16–28.

[40] J. P. Cordebois, F. Sidoroff, Endommagement anisotrope en élasticité et plasticité, Journal de Mécanique Théorique et Appliquée, Numéro spécial (1982) 45–60.

[41] C. Chow, J. Wang, An anisotropic theory of elasticity for continuum damage mechanics, International Journal of Fracture 33 (1) (1987) 3–16.

[42] F. Ghrib, R. Tinawi, Nonlinear behavior of concrete dams using damage mechanics, Journal of Engineering Mechanics 121 (4) (1995) 513–527.

[43] M. Yazdchi, S. Valliappan, W. Zhang, A continuum model for dynamic damage evolution of anisotropic brittle materials, International Journal for Numerical Methods in Engineering 39 (9) (1996) 1555–1583.

[44] K. V. Williams, R. Vaziri, A. Poursartip, A physically based continuum damage mechanics model for thin laminated composite structures, International Journal of Solids and Structures 40 (9) (2003) 2267–2300.

[45] A. Matzenmiller, J. Lubliner, R. L. Taylor, A constitutive model for anisotropic damage in fiber-composites, Mechanics of Materials 20 (2) (1995) 125–152.

[46] J. W. Simon, D. Höwer, B. Stier, S. Reese, J. Fish, A regularized orthotropic continuum damage model for layered composites: intralaminar damage progression and delamination, Computational Mechanics 60 (3) (2017) 445–463.

[47] S. Govindjee, G. J. Kay, J. C. Simo, Anisotropic modelling and numerical simulation of brittle damage in concrete, International Journal for Numerical Methods in Engineering 38 (21) (1995) 3611–3633.

[48] P. Di Re, D. Addessi, E. Sacco, A multiscale force-based curved beam element for masonry arches, Computers & Structures 208 (2018) 17–31.

[49] D. Addessi, S. Marfia, E. Sacco, A plastic nonlocal damage model, Computer Methods in Applied Mechanics and Engineering 191 (13-14) (2002) 1291–1310.

[50] R. De Borst, Simulation of strain localization: a reappraisal of the Cosserat continuum, Engineering Computations (1991).

[51] M. Jirasek, Nonlocal models for damage and fracture: comparison of approaches, International Journal of Solids and Structures 35 (31-32) (1998) 4133–4145.

[52] M. Jirásek, B. Patzák, Consistent tangent stiffness for nonlocal damage models, Computers & Structures 80 (14-15) (2002) 1279–1293.

[53] A. W. Page, P. W. Kleeman, M. Dhanasekar, An in-plane finite element model for brick masonry, in: New Analysis Techniques for Structural Masonry, ASCE, 1985, pp. 1–18.

[54] T. Raijmakers, A. T. Vermeltfoort, Deformation controlled tests in masonry shear walls, Delft: Report B-92-1156, TNO-Bouw (1992).

[55] P. B. Lourenço, Computational strategies for masonry structures. (1997).

[56] D. Addessi, E. Sacco, A multi-scale enriched model for the analysis of masonry panels, International Journal of Solids and Structures 49 (6) (2012) 865–880.

[57] R. Hill, Elastic properties of reinforced solids: some theoretical principles, Journal of the Mechanics and Physics of Solids 11 (5) (1963) 357–372.

[58] A. Zucchini, P. B. Lourenço, A micro-mechanical homogenisation model for masonry: Application to shear walls, International Journal of Solids and Structures 46 (3-4) (2009) 871–886.

# HIGHLIGHTS

- Macromechanical model with damage for analysis of regular masonry is formulated
- Orthotropic behavior and directional strength properties are accounted for
- Novel multisurface damage limit function is proposed
- Nonlocal integral formulation is adopted to avoid mesh-dependency of the FE procedure
- Capability of the model is proved at both material and structural scales

# AUTHORSHIP STATEMENT

Manuscript title:
Orthotropic multisurface model with damage for macromechanical analysis of masonry structures

All persons who meet authorship criteria are listed as authors, and all authors certify that they have participated sufficiently in the work to take public responsibility for the content, including participation in the concept, design, analysis, writing, or revision of the manuscript. Furthermore, each author certifies that this material or similar material has not been and will not be submitted to or published in any other publication before its appearance in the European Journal of Mechanics / A Solids.

**Authorship contributions**

Cristina Gatta:
Methodology, Conceptualization, Formal analysis, Software, Investigation, Validation, Writing - Original Draft, Writing - Review & Editing

Daniela Addessi:
Methodology, Conceptualization, Supervision, Investigation, Writing - Original Draft, Writing - Review & Editing

**Acknowledgements**

All persons who have made substantial contributions to the work reported in the manuscript (e.g., technical help, writing and editing assistance, general support), but who do not meet the criteria for authorship, are named in the Acknowledgements and have given us their written permission to be named. If we have not included an Acknowledgements, then that indicates that we have not received substantial contributions from non-authors.

**This statement is signed by all the authors**

| Author's name (typed) | Author's signature | Date |
|---|---|---|
| Cristina Gatta | Cristina Gatta | March 7, 2023 |
| Daniela Addessi | Daniela Addessi | March 7, 2023 |

**Declaration of interests**

☒ The authors declare that they have no known competing financial interests or personal relationships that could have appeared to influence the work reported in this paper.

☐ The authors declare the following financial interests/personal relationships which may be considered as potential competing interests: